

Designing Radiation Transport Tests: Simulation-Driven Uncertainty-Quantification of the COAX Temperature Diagnostic

C. L. Fryer^{1,2,*}, A. Diaw, C.J. Fontes, A.L. Hungerford, J. Kline, H. Johns, N. E. Lanier, S. Wood, T. Urbatsch¹

Los Alamos National Laboratory, Los Alamos, NM 87545

Abstract

One of the difficulties in developing accurate numerical models of radiation flow in a coupled radiation-hydrodynamics setting is accurately modeling the transmission across a boundary layer. The COAX experiment is a platform design to test this transmission including standard radiograph and flux diagnostics as well as a temperature diagnostic measuring the population of excitation levels and ionization states of a dopant embedded within the target material. Using a broad range of simulations, we study the experimental errors in this temperature diagnostic. We conclude with proposed physics experiments that show features that are much stronger than the experimental errors and provide the means to study transport models.

Keywords: radiation flow

1. Introduction

Laboratory experiments at national laser facilities are designed to probe a wide range of physics include plasma physics, turbulence physics, and radiation flow. For radiation flow, improving the physics in question requires extreme precision. We understand the equations governing this radiation flow; the Boltzman transport equation is believed to accurately represent what happens in nature and we can test our numerical methods in reproducing this equation on

simple problems with existing analytic solutions. To test beyond these analytic comparisons, we must design experiments that move past pure-transport solutions. One example arises from problems testing how radiation couples to matter (both opacities, equation of state and hydrodynamics). The COAX experiment is designed to test one aspect of this problem: the radiation flow across boundary layers.

COAX is the successor to Pleiades, an experiment designed as a first step in studying radiation flow, using a hohlraum drive to study supersonic diffusive flow down a single foam tube constrained by a high opacity wall[11, 6]. This experiment had two sets of diagnostics: soft X-ray spectral emission

*Corresponding Author, fryer@lanl.gov

¹Los Alamos National Laboratory, Los Alamos, NM 87545

²The George Washington University, Washington, DC 20052, USA

of the shock front and a DANTE detection to measure the emergence of the heat front as it emerged from the foam. A surprise in this experiment was that the simulations systematically predicted shorter breakout times for the radiation front through the tube than those measured in the experiment. Although this could be caused by uncertainties in the physics (e.g. most equations of state don't accurately include excitation states of the electrons in the atoms, altering the specific heat), it was found that uncertainties in the experiment could also produce systematic errors[11, 6]. To improve upon this experiment, both a better understanding of the initial conditions and the evolution foam properties (e.g. internal energy) are needed to discriminate between the different interpretations explaining the disagreement between experiment and simulation.

The COAX platform will ultimately include a DANTE diagnostic at the end of the target to measure the breakout time. This DANTE diagnostic has been used extensively at Omega and its uncertainties are well documented[16, 17]. The current design of this platform uses the DANTE detector to measure the hohlraum temperature and a radiograph diagnostic to measure the shock position. However, the primary goal of this paper is to understand the efficacy of a spectral diagnostic to measure the foam temperature in the target. This paper will focus on the sensitivities of this spectral diagnostic.

The spectral diagnostic uses X-ray framing cameras coupled to a four-strip micro-channel plate detector[25] with data collected via film with a 0.002 cm/pixel resolution. Imaging absorption spectroscopy makes it possible to resolve gradients in the material temperature along the direction of

the flow.

The basic design of the COAX experiment includes hohlraum with a laser entrance on one side that drives a radiation flow on the opposite side. The hohlraum is 0.12 cm in height and 0.16 cm in diameter (outer extent) with 0.0025 cm thick walls. The setup uses 13 beams from Omega each delivering 500 J in a 1 ns square pulse with pointings designed to produce a uniform drive through an opening 0.08 cm in diameter into a target. The drive through the hohlraum opening evolves with time, peaking with an effective radiation temperature of 170 eV.

An Aluminum foil (with a thickness of 0.0025 cm) separates the hohlraum from the target to filter out high-energy photons, providing a drive that is closer to the black-body. The target is shown in Figure 1 with two nested foams above a hohlraum drive. The foams are composed of a silicon aerogel with densities near 70 mg cm^{-3} . This foam can be doped with titanium or scandium to provide the spectral absorption features to measure the temperature (e.g. dopants in the form of TiO_2). We have some control of the amount and size of the dopants injected into the foam. The dopants can be placed in either the inner or outer layers. One of the major sources of error in modern radiation transport codes is the treatment of radiation as it crosses a boundary. Varying the foam densities allows experimentalists to alter the boundary conditions to better probe the radiation physics. The experiment and its initial results will be discussed in detail in a later paper (Johns et al., in preparation).

In this paper, we use a suite of simulations to study the sensitivity of this diagnostic to the experimental uncertainties. In particular, we study the uncertainties of

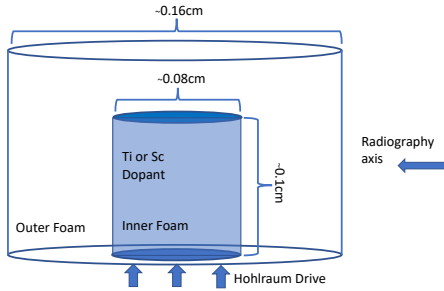


Figure 1: Diagram of the COAX experiment with a two-layer target consisting of an outer and inner foam above a hohlraum drive. The new diagnostic developed in COAX uses titanium or scandium dopants whose spectral signature can be used to measure the temperature of the target. These can be placed in either the inner or outer foams to probe the temperature of the foam and, hence, map out the strength of the radiation front across the foam boundary.

both the initial conditions and the diagnostic itself in the temperature measurement of the diagnostic. Section 2 discusses uncertainties in the initial conditions including uncertainties in both the drive from the hohlraum and the densities in the foam. Section 3 discusses the potential issues with the COAX diagnostic. As we shall see, the diagnostic is fairly insensitive to many uncertainties, but there are some issues that must be understood to fully take advantage of this diagnostic. We conclude with a discussion of the future of the COAX experiment and its ability, given the diagnostic uncertainties, to address key problems in radiation-flow physics.

2. Uncertainties in the Initial Conditions

As with many (if not all) laboratory experiments, uncertainties in the initial conditions can affect the interpretation of the experiment, limiting the ability of these ex-

periments to constrain the physics studied in the experiment. The initial-condition uncertainties were studied in detail in the Pleiades experiment, focusing on the effect of these uncertainties on the position of the shock as a function of time[6]. The COAX temperature diagnostic provides an additional constraint to better understand radiation flow uncertainties. But, as with the Pleiades experiment, we must first understand the level of the uncertainties in the initial conditions on the interpretation of the results from this diagnostic. Like Pleiades, the COAX experiment follows the flow of radiation emitted from a hohlraum through a foam target (Figure 2). The initial-condition uncertainties can be separated into uncertainties in the characteristics of the target, e.g. the foam characteristics (density, composition and inhomogeneities) and uncertainties in the drive (both electron and photons) into this target from the hohlraum (spectrum, angular distribution, luminosity).

Some aspects of these uncertainties studied in the Pleiades experiment have improved in COAX, reducing these associated errors. In addition, instead of studying the uncertainties in the breakout shock, this paper focuses on the uncertainties in the temperature diagnostic developed in COAX. Understanding the effect of these uncertainties is critical in determining what physics we can study with COAX. Although we ultimately want to use the experiments to test the physics implementations in the code, in this paper we use these same codes to determine the extent of the errors from the initial condition uncertainties. For this paper, we use the LANL-ASC code Cassio which includes both implicit Monte Carlo (IMC) and S_N discrete ordinate methods for the radiation transport coupled onto an Eule-

rian adaptive mesh refinement scheme[8].

This study leverages a grid of simulations probing the different uncertainties discussed in this paper. These grids include a set of models that varied the density and the drive using 9 different foam densities ranging from $56 - 77 \text{ mg cm}^{-3}$, 3 drive powers varying the power by $\pm 5\%$, 2 durations varying the duration of the drive by $\pm 10\%$, 2 angles and 2 spectral distributions. We run these models with both Implicit Monte Carlo and S_N options, leading to a total of over a four hundred models in our base grid. We ran a suite of simulations of both angle and energy in the drive for a focused study on these effects (another 20 models). We also ran 20 models varying the foam inhomogeneities (both the density variations and the positions of the inhomogeneities). We ran another suite studying the dopant size (another 20 calculations). In total, this work summarizes the results of over 500 calculations.

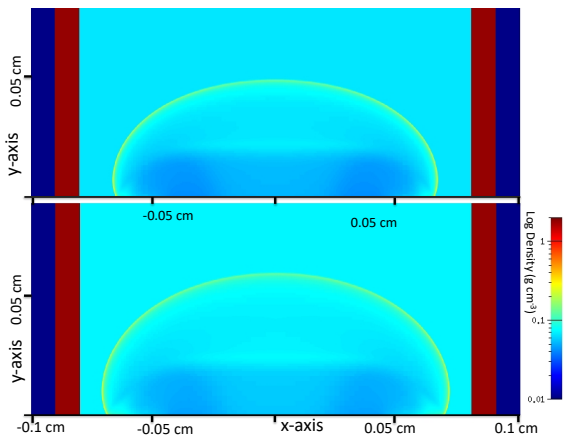


Figure 2: Density map of two simulations of the COAX experiment 2.5 ns after the launch of the drive, varying the density between the upper and lower limits of our $1-\sigma$ error bars.

2.1. Drive

The laser drive itself is generally well-understood with errors less than $\pm 2 - 3\%$.

However, modeling the hohlraum is difficult for codes using the Euler equations as the basis for the hydrodynamics. The Euler equations for momentum, mass and energy conservation implicitly assume matter is in thermal equilibrium. In the low-density conditions of the hohlraum, not only are the ions, electrons and photons decoupled with respect to each other, but these particles tend not to be in equilibrium in parts of the hohlraum[20, 3, 23].

In the hohlraum, such time-independent assumptions are not satisfied, and the calculations are suspect. Simulations can provide a reasonable estimate of the equilibration timescales for different quantities (see appendix). Given the large mean free path of the electrons in both the hohlraum and the target, it is not clear that the electron distribution is a Maxwellian and can be described by a single temperature. If we nonetheless assume the distributions of the ions and the electrons can be described by a Maxwellian, we can then determine the coupling between these two species. We find that the equilibration timescales at 300 eV for electron-ion coupling within the hohlraum and a density of air lie between 1-2 ns and, for near-vacuum densities of 0.03 mg cm^{-3} , 100 ns. The corresponding timescales for the major atomic level states to be within 10% of their time-independent value are on the order of a few ns. Given that the timescales for our COAX experiment is only a few ns, our series of equilibrium and time-independent assumptions is highly suspect for our hohlraum modeling. To date, the primary HEDP codes include minor corrections for out-of-equilibrium physics and time-dependent effects are not included in the atomic level states. This means that most hohlraum models are approximations at best. It is because of these limita-

tions that we have a rather large uncertainty in our drive. The Euler equations used in codes like Hydra [15], RAGE[8] or FLAG[12] do not capture this out-of-equilibrium physics to model the hohlraum and, although they can be used to make a first order estimate of the emission, simulations using these codes can lead to incorrect estimates of averaged terms like heating[3].

Without detailed measurements of the drive coming out of the hohlraum, we are limited to using these first order estimates. To better understand the drive uncertainties, we have conducted a number of studies of electron heating, photon flux and spectrum. Non-thermal electrons produced in the hohlraum can stream into the target, preheating the target material prior to the launch of the radiation front. For low-drive experiments, a few eV pre-heat can alter the evolution of the shock front[5]. But, for the COAX experiment, even a 10 eV pre-heat does not significantly alter the flow of the much more powerful COAX drive. Figure 3 shows the temperature profile of 3 separate simulations at 2 ns with a 1, 5, and 10 eV preheat. The 10 eV preheat (larger than expected from past studies[5]), produces only a small ($\sim 1 - 2$ eV) difference in the profile temperature. Our analysis supports the practice in most radiation transport experiments that this heating is unimportant because both the amount of high-energy emission (electrons and photons) is small compared to the total emission and most of this emission streams through the target.

We have also varied the spectrum and angular distribution of the radiation flowing out of the hohlraum. If all of the photons are non-thermal with temperatures above 1 keV, they can preheat the target, altering the flow. But for a wide range of fluxes (pushing the spectrum above 200 eV

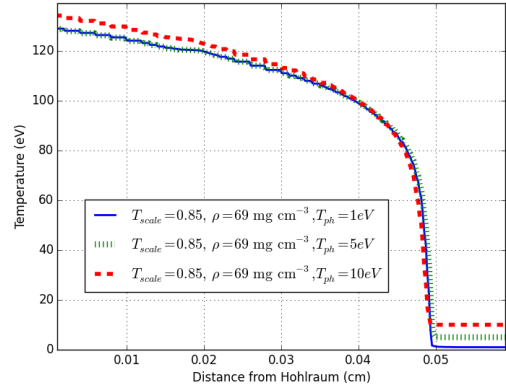


Figure 3: Temperature profile versus distance from the hohlraum drive (0.01 cm from the axis) of our standard drive and density target at 2 ns. We have varied the electron preheat from 1 to 10 eV. This preheat does not change the position of the shock and only a 10 eV preheat makes a noticeable (1 – 2 eV) change in the temperature profile.

or down below 100 eV), the effect is less than a few percent in the shock position and less than 1-2 eV in the temperature profile. Similarly, we produced only small differences when we altered the angular distribution of the radiation flux from a typical Lambertian to a forward-peaked function: $f(\theta) \propto \cos^5(\theta)$. For our drive, the target is sufficiently optically thick to reset the spectral and angular features.

Finally, we varied the power and duration of the radiation emitted from the hohlraum. Figure 4 shows the results for a subset of our grid of calculations where we scale the temperature of the drive by 5% (varying the flux by plus or minus 10%), the duration of the drive by 20% (altering the total energy by plus or minus 10%) and the foam density. The change in power can alter the position of the shock at 2 ns by 0.007 cm or over 10%. The drive duration doesn't alter the forward shock position much but it can alter the temperature behind the shock

which can dominate what we see in the diagnostic measurement. The power and duration alter the temperature by ± 5 eV and ± 7 eV respectively. Combined, the effect is over ± 8 eV. With no constraint on the shock position, the uncertainties in our drive lead to uncertainties in the temperature behind the shock of ± 8 eV. Ideally, we can use the shock position to further constrain the drive. We will discuss this further in our description of the target uncertainties (Sec. 2.2).

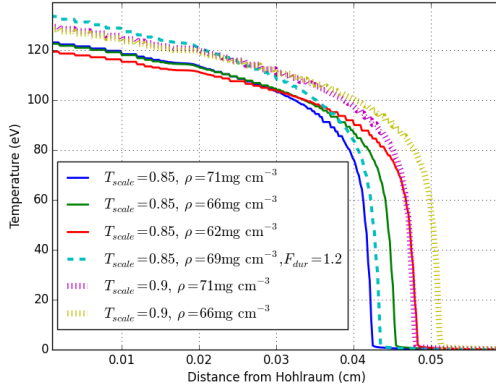


Figure 4: Temperature profile versus distance from the hohlraum drive (0.01 cm from the axis) at 2 ns assuming no preheat and varying both the drive characteristics (duration, power) and foam density. The uncertainties in the drive characteristics lead to an uncertainty in the temperature profile of ± 8 eV. These variations also alter the position of the shock. However, the measured uncertainties in the foam densities can drastically alter the shock position.

2.2. Target Uncertainties

In the Pleiades experiment, foam density measurements typically had 3-4% errors and different measurement techniques produced different results[6]. To study the dependence on density, we varied the density for our COAX experiment from 62 – 71 mg cm^{-3} . By combining these variations

with our drive, we can determine the full errors from our initial conditions. Typically, the density variations alter the position of the shock at a given time with a slightly more modest effect on the temperature profile. In Section 2.1, we pointed out that we might be able to use the shock position to constrain the uncertainties in the drive. However, density uncertainties alter the shock position in a comparable way to the drive uncertainties. With a shock position, we can constrain the drive/density pair, but the uncertainty in the absolute temperature profile remains ± 8 eV. We note, however, that density uncertainties are believed to be smaller for silicon foams and this may overestimate the errors caused by density uncertainties.

In addition to uncertainties in the average foam density, detailed studies of the Pleiades experiment also found that most foams had fairly large scale inhomogeneities in them[6]. For the COAX experiment, we introduce a series of clumps into the foam, keeping the average density constant. Figure 5 shows the density map of a simulation including inhomogeneities. The placement of the inhomogeneities affects both how much the inhomogeneities alter the density map and the arrival times. Figure 6 shows our standard temperature profile map using four different instantiations (different distributions of the clumping) of the density inhomogeneities. Inhomogeneities do not affect the temperature dramatically, but can alter the position of the shock by 10-20%.

With the imaging spectroscopy in COAX, we can not only measure the temperature in the radiation flow, but its slope. For the 6 models presented in figure 4, the slopes are: -674, -615, -530, -816, -596, -597 eV cm^{-1} respectively for the 4 $T_{\text{scale}} = 0.85$ models ($\rho = 77, 66, 62 \text{ gcm}^{-3}$ plus the

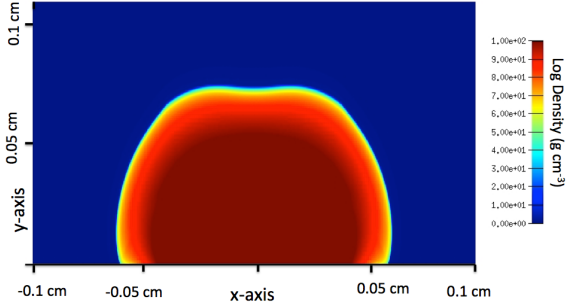


Figure 5: Density map of a COAX experiment simulation 2.0 ns after launch of the drive including inhomogeneities into the target foam but fixing the average foam density. The inhomogeneities can alter the shock front some, but the effect depends sensitively on the placement of the inhomogeneities.

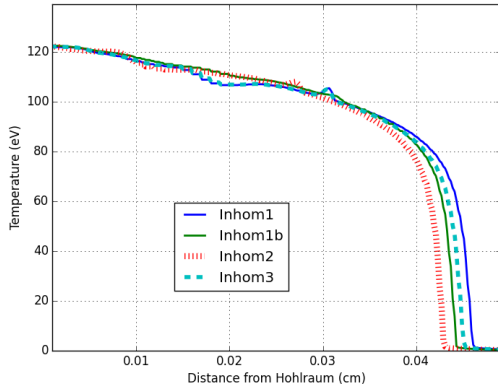


Figure 6: Temperature profile versus distance from the hohlraum drive (0.01 cm from the axis) at 2 ns assuming no preheat for 3 different instantiations of the density inhomogeneities where we varied the geometry of the perturbations but kept the average density constant (Inhom1, Inhom2, Inhom3) with 50% enhancements at the centroids of the perturbation. Inhom1b shows a model where the perturbations are 10% enhancements. Inhomogeneities can alter the shock position by 10-20% and can speed up or slow down the shock.

$\rho = 69 \text{ gcm}^{-3}$, $F_{\text{dur}} = 1.2$ model) and the two $T_{\text{scale}} = 0.9$ models ($\rho = 69, 62 \text{ gcm}^{-3}$). This slope can be used to further distinguish between models. For instance, although the temperatures are very similar between the $T_{\text{scale}} = 0.85$, $\rho = 69 \text{ gcm}^{-3}$, $F_{\text{dur}} = 1.2$ model and the $T_{\text{scale}} = 0.9$, $\rho = 71 \text{ gcm}^{-3}$ model, the temperature gradients are very different. The slope doesn't distinguish between all uncertainties (e.g. the effects of inhomogeneities), but it does provide additional constraints.

Based on the modeling of the Pleiades experiment, these uncertainties are what we expect from foam-based targets and unmeasured hohlraum drives. By including measurements of the shock position, we can constrain some of the degeneracies in our errors, but we can not remove the temperature variations caused by the combined uncertainties. Given the current uncertainties in the drive and target, we can not predict the absolute temperature behind the shock to better than $\pm 8 \text{ eV}$ and, hence, can't confirm this diagnostic's effectiveness to better than $\pm 8 \text{ eV}$. Decreasing the errors in the drive and foam target properties can reduce this uncertainty. In addition, the errors in the relative changes with this diagnostic may be much smaller. To understand this, we must understand the diagnostic uncertainties.

3. Temperature Diagnostic Uncertainties

The temperature diagnostic of the COAX experiment measures the absorption line spectra of a dopant backlit by an X-ray source. As we learned in Section 2, the initial condition uncertainties in this experiment prevent us from validating this probe of the temperature to better than $\pm 8 \text{ eV}$.

We can, however, use simulations to better understand the physics uncertainties of this diagnostic and determine the conditions where it is most effective.

The temperature of the diagnostic is more complex than a simple single-temperature/density profile: the breakdown of equilibrium assumptions, the uniformity of the dopant, and the uniformity of the foam target along the line-of-sight of our X-ray source. In many cases, the deviations caused by these complexities do not affect the accuracy of this diagnostic. We review each of these in turn.

3.1. Equilibration

Although the Cassio code does not assume strict local thermodynamic equilibrium, many of its physics components include equilibrium assumptions. For example, although the code follows both the ion and electron distributions separately, both are assumed to follow a Maxwell-Boltzmann distribution described by a single temperature. The radiation field is followed in multi-group (typically 60-100 groups) following the full Boltzmann transport equation. The opacities typically are set by the electron temperature (assuming radiation and matter equilibrium) in a steady state solution and the time implicit transport scheme relies on these. Different properties of the physics are modeled at different levels of fidelity and equilibrium states. It is worth studying, for our COAX problem, where such a code is valid.

As we have already discussed in Section 2, time-independent, equilibrium assumptions are not justified for all aspects of a laser-driven laboratory experiment. We showed that the conditions in the hohlraum are insufficient to evolve into equilibrium on the timescales of the experiment. But

for the higher densities in the foam target, these assumptions are more valid. The ion-electron equilibration timescales are 0.3 ns for a 60 mg cm^{-3} , 100 eV foam. The electron equilibration times are even shorter. The mean free path of the photons is also low enough for all but the highest energy photons from the drive that the radiation quickly equilibrates as well³. Figure 7 shows the spectrum just behind the radiation front from a 100 group IMC calculation compared to two blackbody profiles. Although the radiation is not a strict blackbody, it is very close to it. The corresponding matter temperature at this time for this tally surface is roughly 80-85 eV, slightly below the radiation temperature as it quickly equilibrates to the radiation.

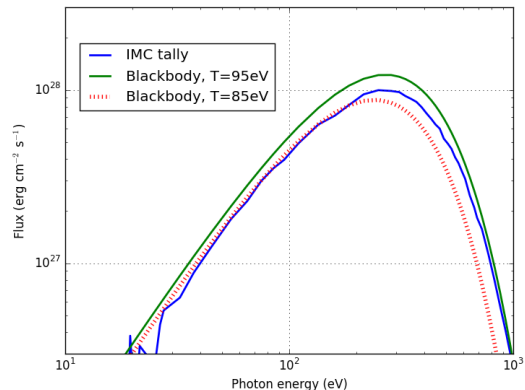


Figure 7: Spectrum (flux versus energy) of the radiation front behind the shock in our COAX simulation compared to two blackbody solutions. Although the spectrum is not a strict blackbody, the variation is minimal. The effective temperature radiation of the radiation is slightly higher than the 80-85 eV matter temperature due to the slight delay in the radiative heating of the matter.

This small variation, both in the black-

³Note that we are assuming the electrons are described by a Maxwellian and this may speed the equilibration of the photons.

body nature of the radiation and the equilibration between radiation and electrons, suggests that the thermodynamic equilibrium can also be assumed for the atomic level states. Indeed, at these high densities, the collision rate is typically high, and the atomic level states reach an equilibrium solution quickly, the corresponding β value measuring the departure from local thermodynamic equilibrium is less than $\sim 0.02 - 0.03$ [4]. Because collisions dominate, any small differences between the radiation spectra and the electron temperature will not affect the level states of our dopant (see Figure 8).

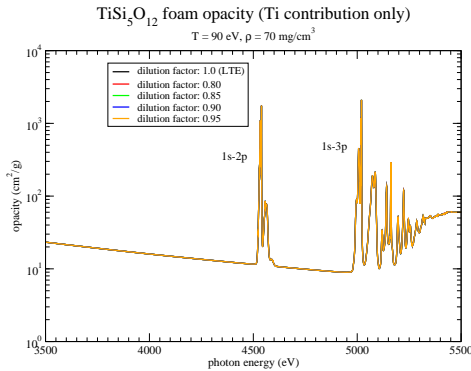


Figure 8: Opacity of the titanium dopant comparing a local thermodynamic equilibrium (LTE) solution to solutions where the radiation flux is reduced or diluted below the LTE temperature. This dilution reduces the role radiation plays in setting the level states. Because collisions dominate the level states, it is not surprising that the spectrum is not affected by this dilution. This calculation assumes that the radiation is described by a single temperature and that the level states are in equilibrium. Although the equilibration time is fast, it is likely that time-dependent effects are more important, especially for measurements made right after the shock has passed.

3.2. Dopant Uniformity

Although the radiation and matter quickly equilibrate in the foam, the equilibration time of the dopant may take longer. For sufficiently large dopant sizes, the timescale to reach an equilibrium temperature is longer than the experimental timescale. This means that the dopant is not necessarily an accurate measure of the temperature of the foam. To test this for our experiment, we have used the adaptive mesh refinement capability in Cassio, we are able to resolve the dopants and determine the timescale for dopants of different size to equilibrate to a uniform temperature. For large dopants ($10 \mu m$), a portion of the dopant would remain cool (< 20 eV) throughout the duration of the experiment. Figure 9 shows the temperature variation for a $1 \mu m$ dopant 0.15 ns and 0.3 ns after the radiation front passes across the dopant. Although the variation is large at 0.15 ns, so is the shock front temperature gradient. The effective radiation temperature and matter temperature are also not in equilibrium at this time and our opacity calculation is not valid. 0.3 ns after the passage of the radiation front, the variation is only 10 eV. Our dopants are typically a fraction of a micron. Figure 10 shows the same variation for a $0.3 \mu m$ dopant. In this case, the dopant has equilibrated within 0.3 ns of the passage of the shock (temperature variations of less than an eV). For the COAX experiment as run, the dopant size is not a source of error.

3.3. Diagnostic Uniformity

Even if the dopants heat quickly and integrate with the foam, our diagnostic traces through a range of conditions and we do not measure a single density/temperature

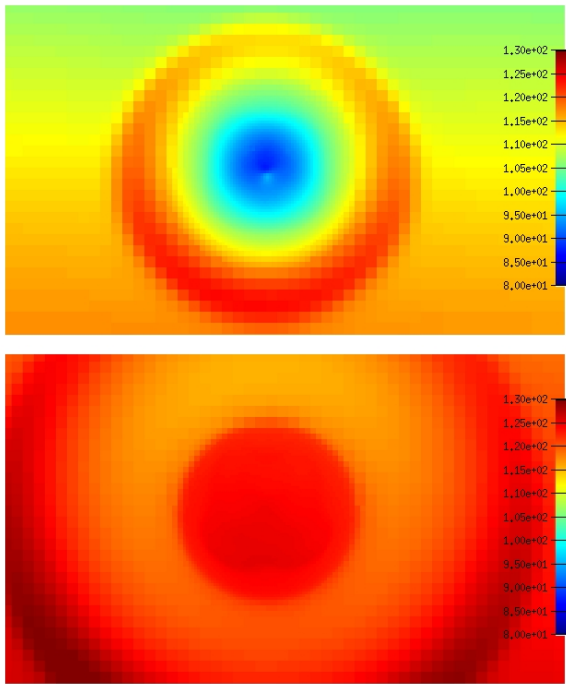


Figure 9: Temperature of a $1\mu m$ dopant 0.15 and 0.3 ns after the radiative front has crossed the dopant. By 0.3 ns, the temperature variation across the doped material is less than 10 eV.

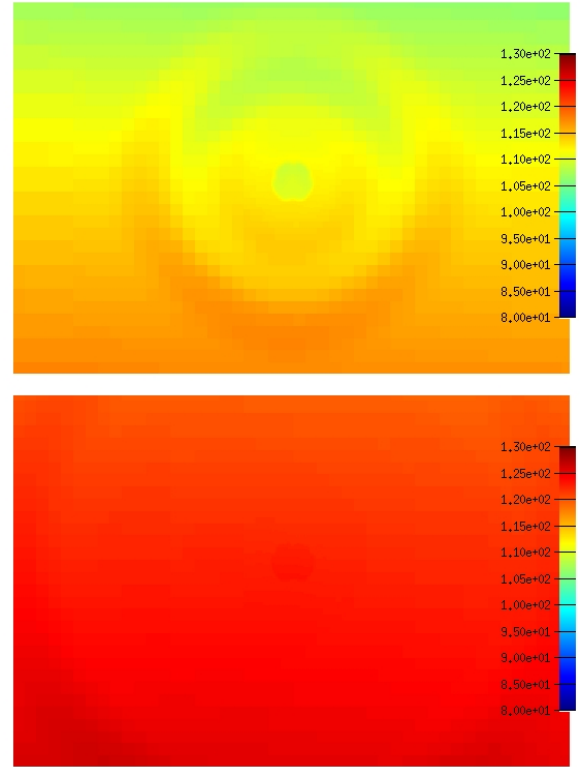


Figure 10: Temperature of a $0.3\mu m$ dopant 0.15 and 0.3 ns after the radiative front has crossed the dopant. By 0.3 ns, the temperature variation across the doped material is less than 1 eV.

condition. The radiation front has a curvature associated with it as it expands laterally (e.g. Figures 2,5). The nature of this curvature will vary with different transport prescriptions and these variations must be extracted from the observed spectra that integrates across the line of site of our experimental diagnostic. Although the analysis is much more difficult than simply assuming a single density/temperature, by understanding and including this variation in our analysis, we can construct a much more accurate diagnostic of the radiation flow.

Figure 11 shows the variation in the temperature distribution across the line of site of the temperature diagnostic as a function of the position and timing of the diagnostic. X-rays produced from a heated krypton source irradiate the target. The curvature in the shock front causes large variations across the target, but we are only concerned with the temperature variations in the doped foam. But even in the doped region, the temperature can vary dramatically (by more than 30%). Similarly, the density in the doped region also has a peak at the shock front (Fig. 12). If the shock front is in the doped region, the density can vary as much as 10-20%. In analyzing this experiment, we introduce errors if we assume our spectra are produced by a single density/temperature pair. However, if we instead use the full temperature and density structures from the simulations to produce spectra, we can compare simulated spectra directly to the diagnostic observation (see Section 3.5). This “forward” analysis approach (using theoretical models to analyze the experiment), using the results of the simulations to compare to the diagnostic measurements, allows us to take advantage of the differences in the temperature profiles and test the differences in transport

techniques more accurately.

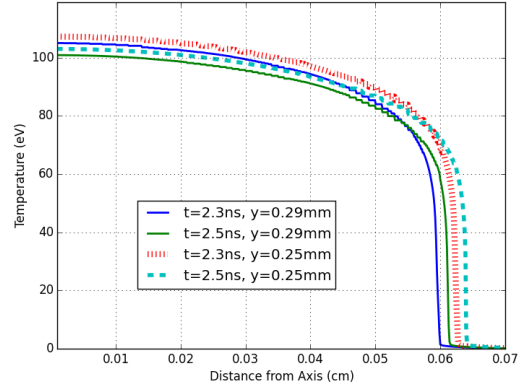


Figure 11: Temperature profile along the line-of-site of the diagnostic X-rays at two different positions (0.025, 0.029 cm above the drive) in our target at 2 different times (2.3, 2.5 ns). Within the doped region, the the temperature varies by over 4 eV. The X-ray diagnostic is actually a slit $30\ \mu\text{m}$ wide that takes data over a 0.1-0.2 ns window. This further broadens the range of temperatures observed in a single data point to $\pm 5\ \text{eV}$.

3.4. Finite Size and Duration of Diagnostic Measurement

Another factor arguing to use simulated profiles to analyze the data from the COAX temperature diagnostic is the fact that the spectra are taken from a slit of finite width (roughly $30\ \mu\text{m}$) and is measured over a finite time ($\sim 0.1 - 0.2\ \text{ns}$). Across the slit at the time of the measurement, the temperature varies by more than $\pm 8\ \text{eV}$ and the density differences vary by more the $\pm 10\%$ (Figures 11,12). By including full simulations in our analysis, we can mitigate these errors as well.

3.5. Modeling Diagnostic Spectra

The variation of temperature and density across the diagnostic measurement caused both by the curvature in the radiation front

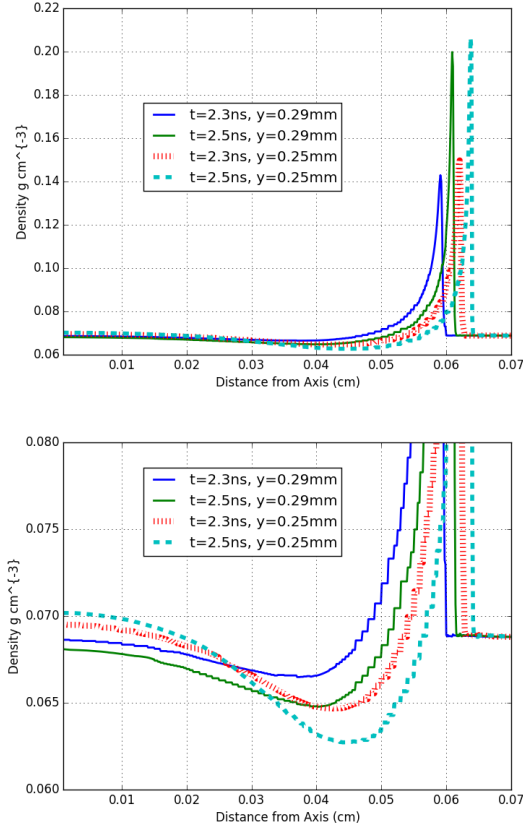


Figure 12: Density profile along the line-of-site of the diagnostic X-rays at two different positions (0.025, 0.029 cm above the drive) in our target at 2 different times (2.3, 2.5 ns). Although, for the most part, the density is flat ($\pm 3\%$) within the doped region, there is a density spike near the radiation front. The densities measured by a single spectrum can also vary by over $\pm 10\%$.

as well as the fact that the diagnostic is not a delta function in width or time. As we have discussed, this requires a forward approach where we calculate simulated spectra and compare directly to the observations (rather than compare inferred temperatures to simulated temperatures). To calculate these spectra, LANL has developed a number of ray-trace algorithms (including absorption and emission) to calculate the transmission from the source. Ray trace methods are ideally suited to our calculations. We can set our line-out to match the ray between the X-ray backlighter and the detector. Although our code includes thermal emission from the target, at the high photon energies of our diagnostic, this emission is negligible. Hence, the X-ray flux through the target ($L_{\text{detected}}(\nu)$) as a function of frequency (ν) is given simply by

$$L_{\text{detected}}(\nu) = L_{\text{source}}(\nu)e^{-\tau(\nu)} \quad (1)$$

where

$$\tau(\nu) = \int_0^W \rho(x)\sigma_\nu(\rho(x), T(x))dx \quad (2)$$

where we integrate along a ray (we assume it is perpendicular to the target so the integration is along width of the target, W), $\sigma_\nu(\rho(x), T(x))$ is the total (scattering plus absorption) opacity in the foam that depends on the composition, density ($\rho(x)$) and temperature ($T(x)$), and $L_{\text{source}}(\nu)$ is the source emission. Figure 13 shows different spectra from our calculations with the full range of possible spectra within these combined experimental errors. Ultimately, combining these uncertainties with our initial conditions uncertainties argue that we can only validate the accuracy of our temperature diagnostic to roughly $\pm 8 - 10$ eV.

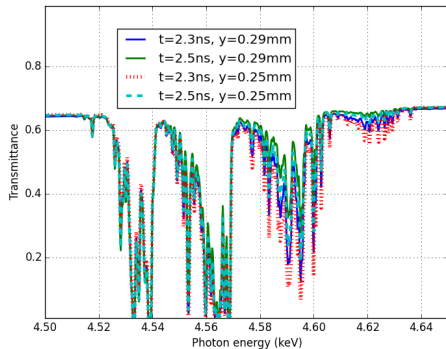


Figure 13: Transmission spectra for our temperature diagnostic along a series of rays varying the position and timing. The diagnostic actually measures a summation of these spectra because of the width of the slit and the duration of the measurement. Although some of the features are strong over all conditions, other features are present in some conditions and absent in others. The sum will produce results in between the values shown here.

4. Next Steps: Applications of the COAX

We have reviewed many of the uncertainties in the COAX radiation flow experiment and its temperature diagnostic. We confirmed that equilibration effects in the target do not introduce uncertainties and, with small enough dopants, there is not a strong stochasticity in the temperature. Our simulations also show that the exact angular distribution and spectrum of the radiation flow do not significantly alter temperature measurements.

However, we have found that uncertainties in the initial conditions (drive, foam target) produce temperature variations at the ± 8 eV level, even if the position of the shock can be used to constrain these conditions. To improve this accuracy, we must measure the drive more carefully. Similarly, the width and time duration of temperature measurement also places a ± 8 eV error on the temperature observed. Combining

these errors (assuming in quadrature), this implies we can validate the temperature diagnostic errors to ± 10 eV.

Whether or not an experiment like COAX can help constrain our numerical models depends upon whether we can a) reduce the initial condition errors and b) design an experiment focused on the differences in the numerical methods. Our error analysis thusfar has modeled the conditions used in the COAX platform development shots. However, the actual COAX experiment includes plans beyond the basic platform shots and, by changing the initial conditions, we might consider the uncertainties in our numerical methods. We highlight these future designs here. The Cassio code is ideally suited to testing the potential for experiments to test transport methods, because both the implicit Monte Carlo and S_N methods were implemented such that the two methods include sources, etc. identically. By switching from one method to the other, we can directly test the differences between transport implementations.

One of the issues with numerical methods in transport is transport across boundary conditions, and the component COAX platform was designed to test this boundary layer modeling. But, to do so, the diagnostic needs to be in the outer shell. Figure 14 compares the temperature along the diagnostic ray-trace for simulations using implicit Monte Carlo and S_N discrete ordinate method. Although the temperature within the doped region from the platform tests is very similar between these two methods, the amount of radiation flowing across the boundary layer is more substantial. The differences are more extreme if we vary the density between the inner and outer region. The largest effect occurs if we decrease the density in the outer layer and this provides

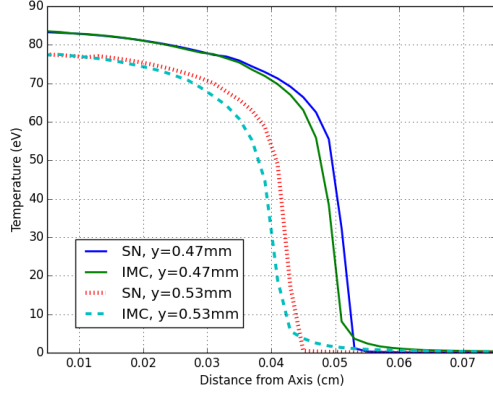


Figure 14: Temperature profile along the line-of-site of the diagnostic X-rays at two different positions (0.047, 0.053 cm above the drive) in our target at 2 different times (3.1, 3.3 ns) and two different drives (solid lines are low drive, dashed lines are high drive). It is possible that the temperature diagnostic, if the dopant were deposited in the outer COAX shell would have a measureable effect.

a good way to test our numerical models for this boundary layer physics. Figure 15 shows the density and temperature profile of the outer shell. The different transport schemes produce profiles that have temperatures that vary by up to 20 eV. The corresponding spectral diagnostic with our doped shell are shown in Figure 16. Even with current errors in the experiment, this difference should be detectable.

One can also broaden how we leverage the COAX platform. As we discussed in our error analysis, large dopants take more time to equilibrate. This again is an example of radiation flow across a boundary and our IMC and S_N results are different. Figure 17 shows the density and temperature profiles across a $10 \mu\text{m}$ dopant 1 ns after the passage of the shock. Work to design an ideal test case for both Omega and NIF platforms is right now underway.

New algorithms are right now being developed to improve the numerics behind

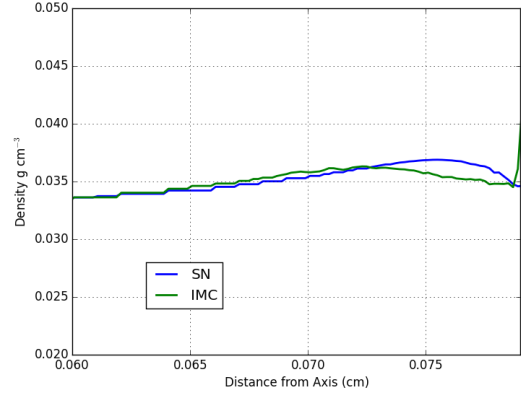
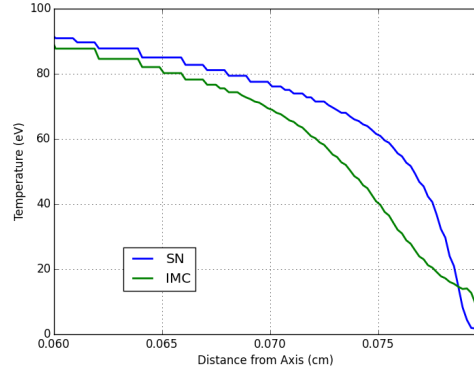


Figure 15: Temperature and density profiles along the line-of-site of the diagnostic for a COAX design where the outer shell density is decreased by a factor of 2.

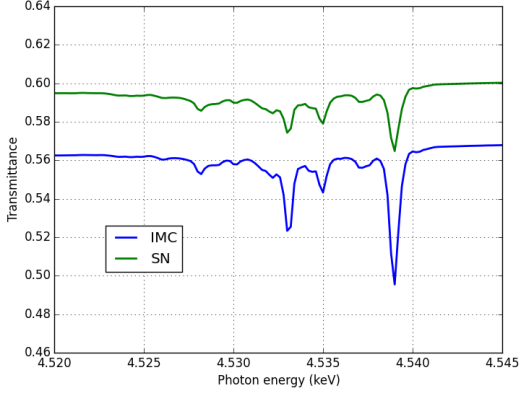


Figure 16: Comparison of our spectral diagnostic between the S_N and IMC simulations of the doped shell. The higher temperature in the S_N simulation leads to stronger line features and higher over-all opacities with respect to the IMC calculation.

boundary transport in codes. With better probes of the output from the hohlraum (underway) and better characterizations of the foam uncertainties, these future COAX experiments are ideally suited to testing these new developments.

Acknowledgements

This work was performed under U.S. Government contract 89233218CNA000001 for Los Alamos National Laboratory (LANL), which is operated by Triad National Security, LLC for the U.S. Department of Energy/National Nuclear Security Administration.

Appendix A. Equilibrium Analysis

To evaluate the electron-ion equilibration times, we use the Landau-Spitzer (LS) electron-ion rate given by [24]:

$$\tau_{ei} = \frac{3}{4\sqrt{2\pi}} \frac{m_e m_j c^3}{n_i Z_i^2 e^4 \lambda} \left(\frac{k_B T_e}{m_e c^2} + \frac{k_B T_i}{m_i c^2} \right)^{3/2} \quad (\text{A.1})$$

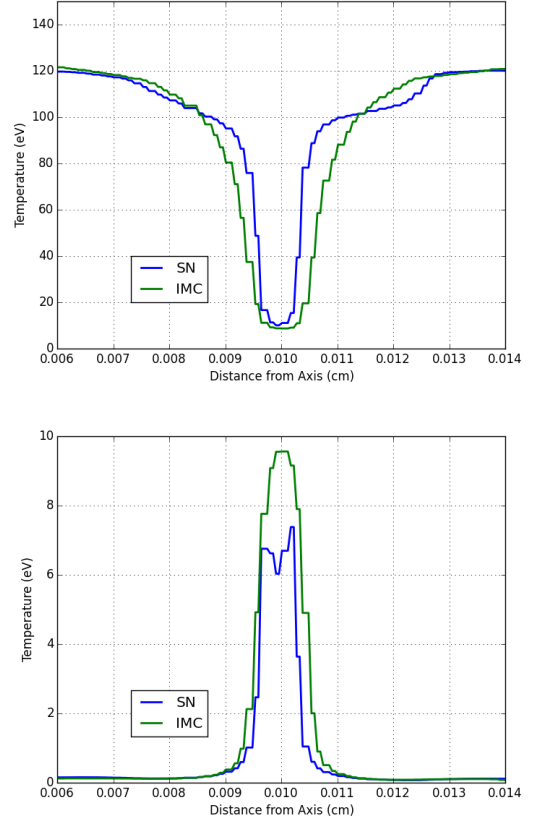


Figure 17: Temperature and density profiles along the line-of-site of the diagnostic across a $10\mu m$ dopant comparing IMC and S_N results. The foam interface is out 0.04 cm and this image focuses on the diffusion beyond this interface where differences in transport methods are most extreme.

Here m_e is the electron mass, m_i the ion mass, k_B is the Boltzman constant, T_e is the electron temperature, T_i is the ion temperature, n_i is the ion density, Z_i is the ion charge number, e is the elementary charge, c is the speed of light, and λ is the Coulomb logarithm containing details of the collision process. The main issue with this rate is finding accurate Coulomb logarithms. Landau-Spitzer used

$$\lambda = \ln \left(\frac{b_{\max}}{b_{\min}} \right) \quad (\text{A.2})$$

where b_{\max} and b_{\min} cutoffs necessary to prevent the divergences that emerge from their treatment. b_{\min} is chosen to be a minimum impact parameter consistent with plasma conditions, such as the classical distance of closest approach

$$b_C = \frac{Z_i e^2}{k_B T_i} \quad (\text{A.3})$$

For systems where quantum degeneracy effects are important b_{\min} is changed to account for quantum diffraction effects by introducing the electron thermal deBroglie wavelength

$$\Lambda = \sqrt{\frac{\hbar^2}{4m_e k_B T_e}} \quad (\text{A.4})$$

where \hbar is the Planck constant, and b_{\max} is chosen to be a screening length occurring from collective plasma effects. A large number of formulae for the Coulomb logarithm exist in the literature. We choose here the expression proposed by Gericke, Murillo, and Schlages (GMS) [7]. Their formula was successfully validated against molecular dynamics simulations results across a wide range of temperature and density [10, 9]. GMS suggested an effective Coulomb logarithm as

$$\lambda = 0.5 \ln \left[1 + \frac{\lambda_D^2 + a_i^2}{\Lambda^2 + b_C^2} \right] \quad (\text{A.5})$$

where the ion sphere radius is given in terms of the ion density n as

$$a_i = \left(\frac{3}{4\pi n} \right)^{1/3} \quad (\text{A.6})$$

Appendix A.1. Timescales in the COAX Experiment

For a pure carbon foam with density $\rho = 60 \text{ mg cm}^{-3}$ and temperature 150 eV, and electron temperature of $T_e = 100$ eV. With the above formula, we estimated the electron-ion relaxation times for a $\text{TiSi}_5\text{O}_{12}$ foam target at temperature of 100 eV for near-vacuum densities ($\rho = 0.03 \text{ mg cm}^{-3}$) and higher density $\rho = 60 \text{ mg cm}^{-3}$ and for an electron temperature of 100 eV. The LS calculations show that the average foam-ion takes around ~ 300 ns to equilibrate with the electrons while for the high density case the equilibration time is around ~ 0.3 ns. Figures 1 and 2 display the electron-foam relaxation predictions from Landau-Spitzer as function of time for two different holhraum densities and temperature.

Appendix A.2. Maxwellianization of Electrons distribution function

Plasmas produced in high energy density experiments are often characterized by steep temperature and density gradients. Because of these gradients, the thermal mean-free path of the electron (λ_{mfp}) becomes large with respect to the characteristic scale length of the temperature $l_T = |T/\nabla T|$. Electrons with mean-free path collisional larger than the scale length of the temperature can escape gradients before being scattered and depositing their energy into the plasma, leading to a distortion of the electrons distribution function (EEDF) away from a Maxwellian distribution [2, 13, 1]. This non-Maxwellian behavior of the EEDF shows the nonequilibrium

behavior of the electron plasma, therefore suggesting the need for a kinetic description for the electrons.

One consequence of the distortions of the EEDF, within hydrodynamics codes, is that the classical Spitzer-Harm formula for the heat-flux can exceed the heat flux of free streaming electrons [21]. Historically, through analysis of experimental results, inertial confinement fusion (ICF) designers very quickly realized this problem of overestimation of the heat flux, and decided to use flux limiter models (which cannot be predictive, and need to be calibrated against experiments), and later nonlocal convolu-

tion kernel to represent the nonequilibrium effects [13, 22, 14].

Recent studies, however, have suggested that for problems relevant to ICF hohlraum conditions, the nonlocal models depart strongly from Vlasov-Fokker-Planck simulations [3, 23]. These observations indicate the need to go beyond equilibrium and near-equilibrium models and adopt kinetic approaches (Boltzmann, Vlasov-Fokker-Planck) to describing electrons dynamics for the near-vacuum hohlraum experiments. Similarly, in these near-vacuum hohlraum experiments ions can also displays non-Maxwellian effects as have been discussed recently in Refs. [19, 18]

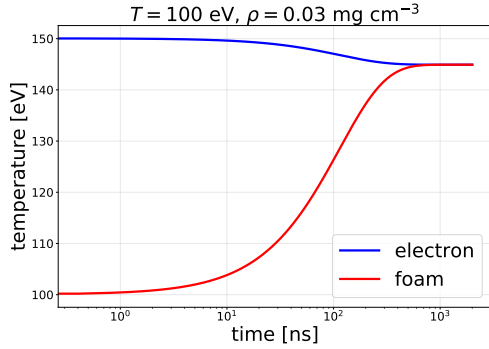


Figure A.18: Electron top curves and foam bottom curves temperature relaxation is shown based on Landa-Spitzer for a density $\rho = 0.03 \text{ mg cm}^{-3}$.

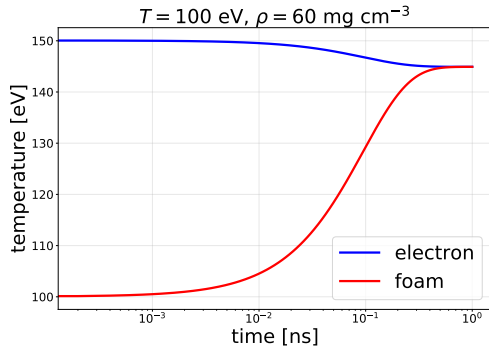


Figure A.19: Same as Fig. A.18 with density $\rho = 60 \text{ mg cm}^{-3}$.

References

- [1] J. R. Albritton, E. A. Williams, I. B. Bernstein, and K. P. Swartz. Nonlocal electron heat transport by not quite Maxwell-Boltzmann distributions. *Physical Review Letters*, 57: 1887–1890, October 1986. doi: 10.1103/PhysRevLett.57.1887.
- [2] A. R. Bell. Electron energy transport in ion waves and its relevance to laser-produced plasmas. *Physics of Fluids*, 26:279–284, January 1983. doi: 10.1063/1.864018.
- [3] J. P. Brodrick, R. J. Kingham, M. M. Marinak, M. V. Patel, A. V. Chankin, J. T. Omotani, M. V. Umansky, D. Del Sorbo, B. Dudson, J. T. Parker, G. D. Kerbel, M. Sherlock, and C. P. Ridgers. Testing nonlocal models of electron thermal conduction for magnetic and inertial confinement fusion applications. *Physics of Plasmas*, 24(9):092309, September 2017. doi: 10.1063/1.5001079.
- [4] M. Busquet. Radiation-dependent ionization model for laser-created plasmas. *Physics of Fluids B*, 5:4191–4206, November 1993. doi: 10.1063/1.860586.
- [5] K. Falk, M. Holec, C. J. Fontes, C. L. Fryer, C. W. Greeff, H. M. Johns, D. S. Montgomery, D. W. Schmidt, and M. Šmíd. Measurement of Preheat Due to Nonlocal Electron Transport in Warm Dense Matter. *Physical Review*

- Letters*, 120(2):025002, January 2018. doi: 10.1103/PhysRevLett.120.025002.
- [6] C. L. Fryer, E. Dodd, W. Even, C. J. Fontes, C. Greeff, A. Hungerford, J. Kline, K. Musack, I. Tregillis, J. B. Workman, J. Benstead, T. M. Guymer, A. S. Moore, and J. Morton. Uncertainties in radiation flow experiments. *High Energy Density Physics*, 18:45–54, March 2016. doi: 10.1016/j.hedp.2016.01.003.
 - [7] D. O. Gericke, M. S. Murillo, and M. Schlanges. Dense plasma temperature equilibration in the binary collision approximation. *Phys. Rev. E*, 65:036418, Mar 2002. doi: 10.1103/PhysRevE.65.036418.
 - [8] M. Gittings, R. Weaver, M. Clover, T. Betlach, N. Byrne, R. Coker, E. Dendy, R. Hueckstaedt, K. New, W. R. Oakes, D. Ranta, and R. Stefan. The RAGE radiation-hydrodynamic code. *Computational Science and Discovery*, 1(1):015005, October 2008. doi: 10.1088/1749-4699/1/1/015005.
 - [9] J. N. Glosli, F. R. Graziani, R. M. More, M. S. Murillo, F. H. Streitz, M. P. Surh, L. X. Benedict, S. Hau-Riege, A. B. Langdon, and R. A. London. Molecular dynamics simulations of temperature equilibration in dense hydrogen. *Phys. Rev. E*, 78:025401, Aug 2008. doi: 10.1103/PhysRevE.78.025401.
 - [10] F. R. Graziani, V. S. Batista, L. X. Benedict, J. I. Castor, H. Chen, S. N. Chen, C. A. Fichtl, J. N. Glosli, P. E. Grabowski, A. T. Graf, S. P. Hau-Riege, A. U. Hazi, S. A. Khairallah, L. Krauss, A. B. Langdon, R. A. London, A. Markmann, M. S. Murillo, D. F. Richards, H. A. Scott, R. Shepherd, L. G. Stanton, F. H. Streitz, M. P. Surh, J. C. Weisheit, and H. D. Whitley. Large-scale molecular dynamics simulations of dense plasmas: The Cimarcon Project. *High Energy Density Physics*, 8: 105–131, March 2012. doi: 10.1016/j.hedp.2011.06.010.
 - [11] T. M. Guymer, A. S. Moore, J. Morton, J. L. Kline, S. Allan, N. Bazin, J. Benstead, C. Bentley, A. J. Comley, J. Cowan, K. Flippo, W. Garbett, C. Hamilton, N. E. Lanier, K. Musack, K. Obrey, L. Reed, D. W. Schmidt, R. M. Stevenson, J. M. Taccetti, and J. Workman. Quantifying equation-of-state and opacity errors using integrated supersonic diffusive radiation flow experiments on the National Ignition Facility. *Physics of Plasmas*, 22(4):043303, April 2015. doi: 10.1063/1.4919025.
 - [12] A. K. Harrison, M. J. Shashkov, J. Fung, J. R. Kamm, and T. R. Canfield. Development of a sub-scale dynamics model for pressure relaxation of multi-material cells in Lagrangian hydrodynamics. In *European Physical Journal Web of Conferences*, volume 10 of *European Physical Journal Web of Conferences*, page 00039, 2010. doi: 10.1051/epjconf/201010000039.
 - [13] J. F. Luciani, P. Mora, and J. Virmont. Non-local heat transport due to steep temperature gradients. *Physical Review Letters*, 51: 1664–1667, October 1983. doi: 10.1103/PhysRevLett.51.1664.
 - [14] W. Manheimer, D. Colombant, and V. Goncharov. The development of a Krook model for nonlocal transport in laser produced plasmas. I. Basic theory. *Physics of Plasmas*, 15(8): 083103, August 2008. doi: 10.1063/1.2963078.
 - [15] M. M. Marinak, G. D. Kerbel, N. A. Gentile, O. Jones, D. Munro, S. Pollaine, T. R. Dittrich, and S. W. Haan. Three-dimensional HYDRA simulations of National Ignition Facility targets. *Physics of Plasmas*, 8:2275–2280, May 2001. doi: 10.1063/1.1356740.
 - [16] M. J. May, K. Widmann, C. Sorce, H. S. Park, and M. Schneider. Uncertainty analysis technique for OMEGA Dante measurements). *Review of Scientific Instruments*, 81(10):10E505, Oct 2010. doi: 10.1063/1.3475385.
 - [17] M. J. May, J. R. Patterson, C. Sorce, K. Widmann, K. B. Fournier, and F. Perez. Source geometric considerations for OMEGA Dante measurements). *Review of Scientific Instruments*, 83(10):10E117, Oct 2012. doi: 10.1063/1.4734041.
 - [18] H. G. Rinderknecht, P. A. Amendt, M. J. Rosenberg, C. K. Li, J. A. Frenje, M. Gatu Johnson, H. Sio, F. H. Séguin, R. D. Petrasso, A. B. Zylstra, G. Kagan, N. M. Hoffman, D. Svyatsky, S. C. Wilks, V. Y. Glebov, C. Stoeckl, and T. C. Sangster. Ion kinetic dynamics in strongly-shocked plasmas relevant to ICF. *Nuclear Fusion*, 57(6):066014, June 2017. doi: 10.1088/1741-4326/aa69d9.
 - [19] H. G. Rinderknecht, P. A. Amendt, S. C. Wilks, and G. Collins. Kinetic physics in ICF: present understanding and future directions.

- Plasma Physics and Controlled Fusion*, 60(6): 064001, June 2018. doi: 10.1088/1361-6587/aab79f.
- [20] H. G. Rinderknecht, P. A. Amendt, S. C. Wilks, and G. Collins. Kinetic physics in ICF: present understanding and future directions. *Plasma Physics and Controlled Fusion*, 60(6): 064001, June 2018. doi: 10.1088/1361-6587/aab79f.
 - [21] M. D. Rosen, H. A. Scott, D. E. Hinkel, E. A. Williams, D. A. Callahan, R. P. J. Town, L. Divol, P. A. Michel, W. L. Kruer, L. J. Suter, R. A. London, J. A. Harte, and G. B. Zimmerman. The role of a detailed configuration accounting (DCA) atomic physics package in explaining the energy balance in ignition-scale hohlraums. *High Energy Density Physics*, 7:180–190, September 2011. doi: 10.1016/j.hedp.2011.03.008.
 - [22] G. P. Schurtz, P. D. Nicolaï, and M. Busquet. A nonlocal electron conduction model for multidimensional radiation hydrodynamics codes. *Physics of Plasmas*, 7:4238–4249, October 2000. doi: 10.1063/1.1289512.
 - [23] M. Sherlock, J. P. Brodrick, and C. P. Ridgers. A comparison of non-local electron transport models for laser-plasmas relevant to inertial confinement fusion. *Physics of Plasmas*, 24(8): 082706, August 2017. doi: 10.1063/1.4986095.
 - [24] L. Spitzer. *Physics of Fully Ionized Gases*. 1962.
 - [25] J. M. Taccetti, P. A. Keiter, N. Lanier, K. Mussack, K. Belle, B. G. Devolder, and G. R. Magelssen. Measuring the Propagation of a Supersonic Radiation Front in Foam via Spatially Resolved Spectral Imaging of a Tracer Layer. In *APS Division of Plasma Physics Meeting Abstracts*, volume 52 of *APS Meeting Abstracts*, page NP9.159, Nov 2010.